RESEARCH

Magnetic, biocompatible $FeCO_3$ nanoparticles for T2-weighted magnetic resonance imaging of in vivo lung tumors

Suresh Thangudu[1], Chun-Chieh Yu[1], Chin-Lai Lee[1], Min-Chiao Liao[1] and Chia-Hao Su[1,2,3*]

Abstract

Background: Late diagnosis of lung cancer is one of the leading causes of higher mortality in lung cancer patients worldwide. Significant research attention has focused on the use of magnetic resonance imaging (MRI) based nano contrast agents to efficiently locate cancer tumors for surgical removal or disease diagnostics. Although contrast agents offer significant advantages, further clinical applications require improvements in biocompatibility, biosafety and efficacy.

Results: To address these challenges, we fabricated ultra-fine Iron Carbonate Nanoparticles ($FeCO_3$ NPs) for the first time via modified literature method. Synthesized NPs exhibit ultra-fine size (~ 17 nm), good dispersibility and excellent stability in both aqueous and biological media. We evaluated the MR contrast abilities of $FeCO_3$ NPs and observed remarkable T2 weighted MRI contrast in a concentration dependent manner, with a transverse relaxivity (r2) value of 730.9 ± 4.8 mM^{-1} S^{-1} at 9.4 T. Moreover, the r2 values of present $FeCO_3$ NPs are respectively 1.95 and 2.3 times higher than the clinically approved contrast agents Resovist® and Friedx at same 9.4 T MR scanner. $FeCO_3$ NPs demonstrate an enhanced T2 weighted contrast for in vivo lung tumors within 5 h of post intravenous administration with no apparent systemic toxicity or induction of inflammation observed in in vivo mice models.

Conclusion: The excellent biocompatibility and T2 weighted contrast abilities of $FeCO_3$ NPs suggest potential for future clinical use in early diagnosis of lung tumors.

Keywords: Metal carbonates, Magnetic resonance, T2 weighted contrast, In vivo lung tumors, Biosafety
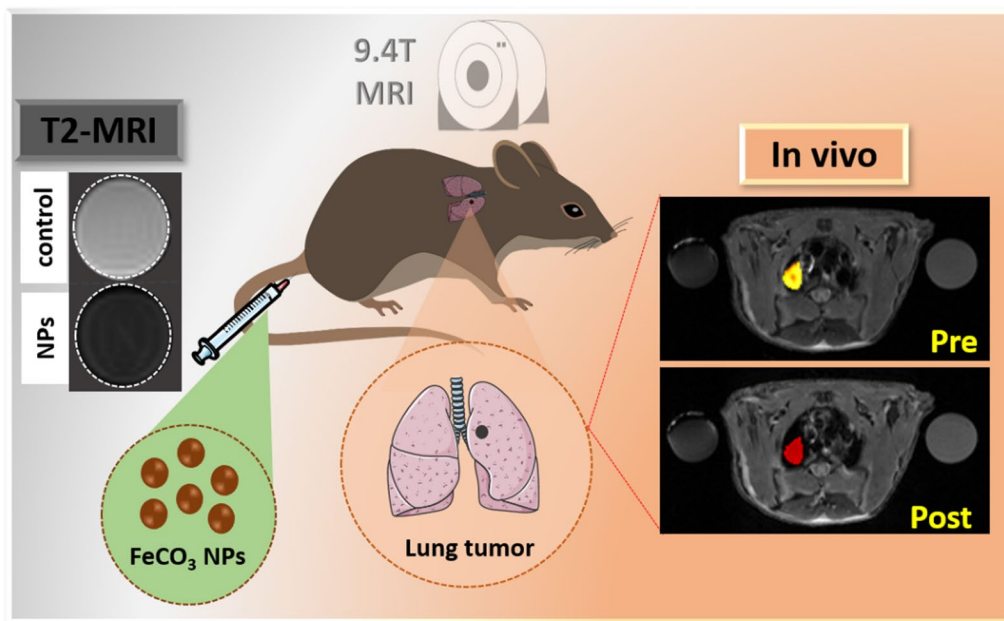
*Correspondence: chiralsu@gmail.com
[1] Institute for Translational Research in Biomedicine, Kaohsiung Chang Gung Memorial Hospital, Kaohsiung 833, Taiwan
Full list of author information is available at the end of the article

Graphical Abstract

Background

Lung carcinoma causes high rates of mortality worldwide, with nearly 2.1 million diagnoses and 1.8 million deaths in 2018 [1]. Despite the availability of surgical removal, cytotoxic chemotherapy, and radiation therapy, long-term survival rates are still below 15% [2]. To date, surgery remains the primary intervention for early diagnosed lung cancers [3]. Unfortunately, surgery is less effective in late-stage lung cancer patients due to the uncontrolled invasion and metastasis of lung tumors and the difficulty of complete excision without leaving microscopic tumors behind. More than 20% of early-diagnosed lung cancers are inoperable due to advanced patient age, severely impaired lung function, and other comorbidities. The key factor in higher mortality in lung cancer patients is late diagnosis. This raises an urgent need for an alternative approach to successfully diagnosis lung tumors in an early stage. To this end, imaging modalities such as X-ray computed tomography (CT), positron emission tomography (PET), and magnetic resonance imaging (MRI) offer significant hope for efficient clinical tumor detection [4]. Among these imaging modalities, magnetic resonance imaging (MRI) has a critically important role in molecular imaging and clinical diagnosis because it is non-invasive, offers excellent soft tissue contrast and can produce images with high spatial and temporal resolution (Additional file 1: Table S1) [5, 6]. However, approximately 35% of clinical MR scans require contrast agents to further improve sensitivity and diagnostic accuracy [7, 8]. Paramagnetic gadolinium (Gd^{3+}) chelates have been extensively used as T1 weighted contrast agents in MRI to further enhance diagnostic accuracy with significant clinical outcomes [9]. However, the United States Food and Drug Administration (USFDA) has warned against the usage of Gd-based contrast agents because of the potential risk of side effects such as nephrogenic systemic fibrosis and kidney dysfunction [10, 11]. Therefore, it is highly desirable to develop a novel alternative to Gd^{3+} chelates.

Increased research attention has focused on superparamagnetic iron oxide nanoparticle (SPION)-based T2 contrast agents due to their nontoxicity and biodegradability [12, 13]. The USFDA approved the Resovist® and Friedx formulations for use as T2 weighted MR contrast agents in clinical applications [14, 15], but they were subsequently recalled following a re-evaluation of safety and efficacy [16]. To address the safety issues, surface modification ligands such as polyethylene glycol (PEG), polysaccharides, peptides or dextran were coated on SPIONs and examined at both in vitro and in vivo levels [17–19]. Despite offering good biocompatibility, such a coating on SPION may increase the hydrodynamic size and diminish the efficacy of the particles' magnetic contrast

Thangudu *et al. Journal of Nanobiotechnology*   (2022) 20:157

Page 3 of 13
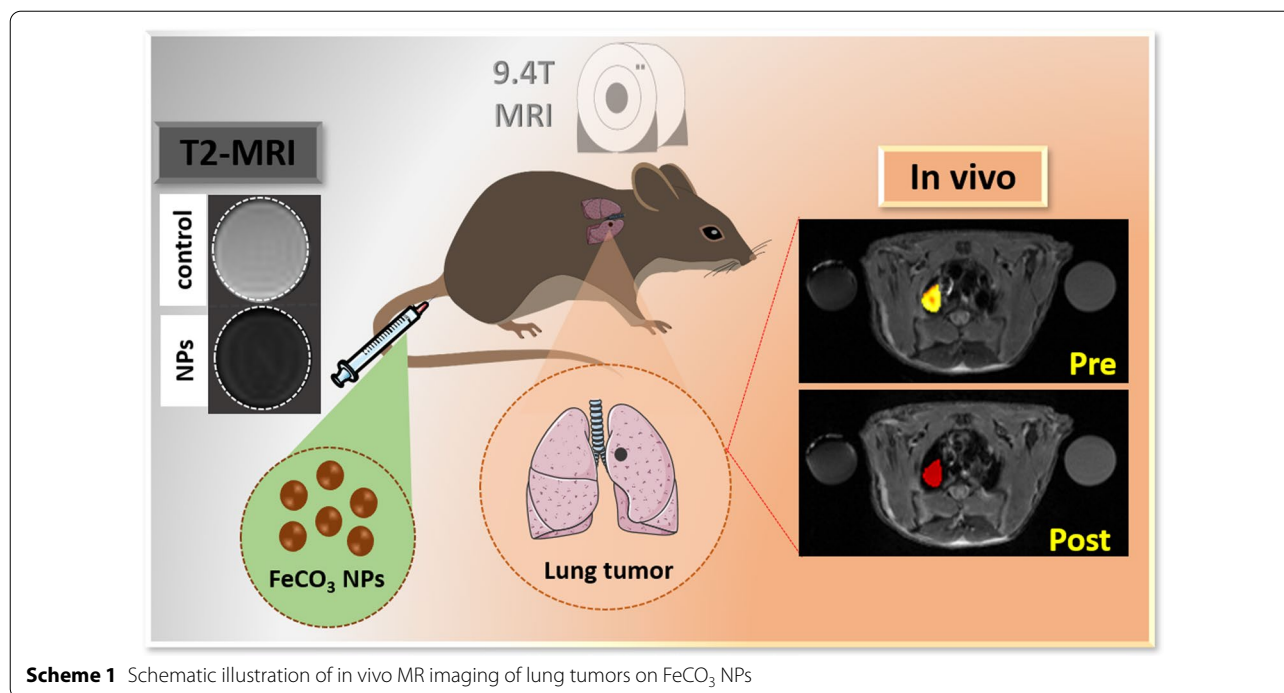
Scheme 1 Schematic illustration of in vivo MR imaging of lung tumors on FeCO$_3$ NPs

abilities [20]. Thus, it is imperative to develop a novel T2 weighted contrast agent with high relaxivity, sensitivity and excellent biocompatibility for high-performance MRI diagnosis. Recently, metal carbonates, specifically calcium carbonate (CaCO$_3$)-based nanomaterials (NMs) have been widely used in biomedical applications, offering improved biocompatibility, biodegradability, and biosafety [21–23]. CaCO$_3$ coated/co-doped magnetic nanoparticles were fabricated and used in an MRI-guided theranostic platform for treating tumors with significant outcomes [24–26]. However, surface coated/co-doped CaCO$_3$ will decompose under the acidic pH conditions in tumors, raising serious questions about the intrinsic toxicity and biocompatibility of loaded NMs. Thus, a direct magnetic metal carbonate nanoformulation offers a promising alternative to overcome the existing limitations and minimize side effects. As a result, manganese metal carbonates (MnCO$_3$) such as MnCO$_3$@PDA [27], MnCO$_3$@PEA [28] were successfully utilized as T1 weighted MR contrast agents for in vivo subcutaneous tumors, offering acidic pH-triggered contrast ability with no cytotoxicity. However, surface coating ligands on the nanoformulations are still a considerable factor for MR contrast properties. In contrast, direct magnetic metal carbonates as a T2-weighted MR contrast agents have not yet been reported in the literature. The present work reports the first fabrication of ultra-fine FeCO$_3$ NPs for T2 weighted in vivo real-time MR imaging of lung tumors. The synthesized FeCO$_3$ NPs exhibit

enhanced T2 weighted contrast abilities with an r2 value of 730.9 ± 4.8 mM^{-1} S^{-1}, a significant improvement on clinically approved contrast agents. Furthermore, the proposed FeCO$_3$ NPs offer remarkable T2-weighted enhancement in both in vitro and in vivo systems. Notably, tumor specific contrast of $\geq 85\%$ was achieved within 5 h post injection of FeCO$_3$ NPs via intravenous (iv) administration in lung tumors implanted in mice models. Furthermore, biosafety data reveals that proposed FeCO$_3$ NPs are biocompatible with no significant toxic effects to the function of major organs such as liver or kidney. Overall, results suggest that the present biocompatible, non-toxic FeCO$_3$ NPs are an excellent choice for future clinical detection of lung tumors. A schematic illustration of the in vivo T2-weighted MR imaging of lung tumors on as-synthesized FeCO$_3$ NPs is shown in Scheme 1.

Materials and methods
Materials
Ferric chloride hexahydrate (FeCl$_3$·6H$_2$O), sodium carbonate (Na$_2$CO$_3$), and ascorbic acid (AA) were purchased from Sigma-Aldrich at highest available purity and used without further purification.

Synthesis of FeCO$_3$ NPs
Briefly, 4 mmol of FeCl$_3$·6H$_2$O was added to 50 mL distilled water and stirred for 30 min at room temperature. After dissolving completely, 24 mL of 0.5 M Na$_2$CO$_3$ aqueous solution was added slowly. After that, 5.3 mmol

of AA was added to the above solution and stirred for 30 min at room temperature. After 30 min, the reaction solution was transferred into a 100 mL Teflon lined autoclave and heated for 12 h at 160 ℃, after which the reaction was cooled to room temperature and washed with ethanol and water several times, followed by drying at 60 ℃ for 6 h, producing micrometer-scale $FeCO_3$. To achieve a nano-sized $FeCO_3$, the resulting particles were dispersed in deionized water and centrifuged at 6000 rpm for 5 min. Finally, a supernatant solution containing $FeCO_3$ NPs were collected and further stored at room temperature for further applications.

Evaluation of T1/T2 contrast abilities of FeCO$_3$ NPs
Aqueous solutions with different concentrations of $FeCO_3$ NPs (between 0 to 0.1 mM, concentration respective to Fe) were diluted with a 1:1 water agar mixture and subsequently evaluated for T1 and T2-weighted MR imaging using a 9.4 T MRI instrument with a head coil (Biospec 94/20, Bruker, Ettingen, Germany). Furthermore, r1 and r2 relaxivity values were obtained by plotting the relaxation time $1/T1/T2$ (s^{-1}) vs the molar concentration of Iron (mM).

In vitro cytotoxicity assay of FeCO$_3$ NPs in normal cells
MRC-5 normal cells (human fetal lung fibroblast cells) were seeded in 96-well plates at a density of 1×10^4 cells per well. After 24 h, different concentrations (0, 10, 25, 50, 75, 100, 150, 200 µg/mL) of $FeCO_3$ NPs were added to the cells and incubated for 24 and 48 h. Thereafter, 20 µL of CCK-8 reagent was added into each well and further incubated for 4 h at 37 ℃ and 5% CO_2. Absorbance (at 450 nm) of each well was then recorded using an ELISA reader (Thermo scientific, Hudson, NH). Mean and standard deviation (SD) were calculated from three parallel readings.

Hemolysis assay
To collect the red blood cells (RBC), 5 mL of mice blood was obtained and centrifuged at 2500 rpm (5 min) and then washed with PBS three times. The resulting RBCs were suspended in 40 mL of PBS and stored at 4 ℃ for further usage. Later, different concentrations of the $FeCO_3$ NPs were added to 0.5 mL of the RBC solution and incubated for 2 h at room temperature. For comparison, PBS and deionized water were respectively used as negative and positive controls. After 2 h of incubation, all samples were centrifuged, and the absorption of the resulting supernatants was measured at 561 nm. From the absorption results, we estimated the hemolysis percentage using following equation: Hemolysis rate = $[(OD_{samples} - OD_{negative})/(OD_{positive} - OD_{negative}) \times 100\%]$ [29].

In vitro MR contrast abilities of FeCO$_3$ NPs
Different concentrations of $FeCO_3$ NPs (0, 15, 70, 140 mM, respective to Fe ion) were incubated with the pre-seeded lung cancer cells (CL1-5-luc/GFP) (3×10^5 cells per well). After 24 h of incubation, the cell pellets were washed with PBS and dispersed in the 1:1 agarose deionized water mixture solution to evaluate the T2-weighted MR imaging using a 9.4 T MRI instrument with a head coil (Biospec 94/20, Bruker, Ettingen, Germany).

Animal models
NOD/SCID nude mice (male, 8–10 weeks old) and BALB/c mice (male, 8–10 weeks old) were purchased from the Experimental Animal Center of the National Science Council, Taiwan. The mice were housed under temperature control (24–25 ℃) and a 12-h light–dark cycle (lights on at 07:00) at the Chang Gung Memorial Hospital Laboratory Animal Center which is accredited by the Association for Assessment and Accreditation of Laboratory Animal Care.

Establishment of lung tumors in animal models
In vivo imaging studies were performed on NOD/SCID nude mice (male, 8–10 weeks old). All experimental protocols involving live animals were reviewed and approved by the Institutional Animal Care and Use Committee (IACUC No. 2021031802) of Chang Gung Memorial Hospital and were performed in accordance with the Animal Protection Regulations of the Council of Agriculture, Executive Yuan (R.O.C.) and the guidelines of National Research Council (USA) for the care and use of laboratory animals. For lung tumor implantation, mice were anesthetized using an intraperitoneal injection of Zoletil® (Virbac, France) and placed in a face-up position. A solution of 10 µL RPMI-1640 medium (5×10^4 CL1-5-Luc/GFP cells) and 10 µL Basement Membrane Matrix (BD, USA) was directly injected (3 mm depth) into the right lung of the mice via BD Insulin Syringes 30G 3/10 cc (BD, USA).

IVIS imaging system for tumor monitoring
Fourteen days following tumor implantation, bioluminescence flux was monitored to assess tumor growth by intraperitoneal injection of D-Luciferin (Caliper Life Sciences). Ten minutes following D-Luciferin injection, mice were subjected to IVIS bioluminescence (emission = 560 nm) imaging (PerkinElmer, Waltham, MA, USA) and the resulting images were analyzed using living imaging software with a pseudo color image representing the tumor.

Thangudu *et al. Journal of Nanobiotechnology*   (2022) 20:157

Page 5 of 13

Evaluating the T2 weighted MR efficacy of $FeCO_3$ NPs in lung tumor animal models

Lung tumor-bearing mice were first anesthetized and an aqueous solution of $FeCO_3$ NPs (10 mg Fe/kg) was intravenously injected into each mouse, followed by scanning with a 9.4 T MRI scanner (Biospec 94/20, Bruker, Ettingen, Germany) with a transmit-receive volume coil (75/40 mm). MR images were collected both pre- and post-injection (1 h, 3 h and 5 h). To obtain higher resolution T2-weighted images (both coronal and axial), we used the multislice turbo rapid acquisition with refocusing echoes (Turbo-RARE) sequence with the following parameters: field of view (FOV) $= 35.0 \times 35.0$ mm; matrix size $= 192 \times 192$; spatial resolution $= 182 \times 182$ µm; slice thickness $= 1$ mm; effective echo time (TE) $= 15$ ms; echo time $= 15$ ms; repetition time (TR) $= 1000$ ms; rare facto $= 2$; refocusing flip angle $= 180º$; number of averages $= 1$; number of repetitions (NR) $= 1$. All images were acquired with respiration and ECG trigger using Amira software, version 2020.2.

Histological examination

Five days following the administration of $FeCO_3$, the animals were sacrificed and heart, liver, spleen, lung, kidney, and tumor tissues from the representative mice in each group were sectioned into slices for H&E TUNEL staining analysis. The stained slices were examined using an optical microscope for detailed observations of histological changes in the organs.

Measurement of liver and kidney function assay

For liver and kidney function analysis, adult male BALB/c mice were used. Five days following $FeCO_3$ NPs (10 mg Fe ion/kg of mice) injection, blood was collected from the retro-orbital sinus at specified time points. Liver and kidney activity was assessed by measuring the serum ALT, ASP, BUN, CRE levels by using a Hitachi Type 717 automatic analyzer (Hitachi).

Statistical analysis

All data are presented as the mean $\pm$ standard deviation, comparing groups using the student's t test or one-way ANOVA using GraphPad Prism 5 Software (Graph-Pad Software, Inc., San Diego, CA, USA). A P value of < 0.05 was considered statistically significant. *$P < 0.05$; **$P < 0.01$; ***$P < 0.001$. n $= 3$ number of mice was used for each in vivo treatment groups.
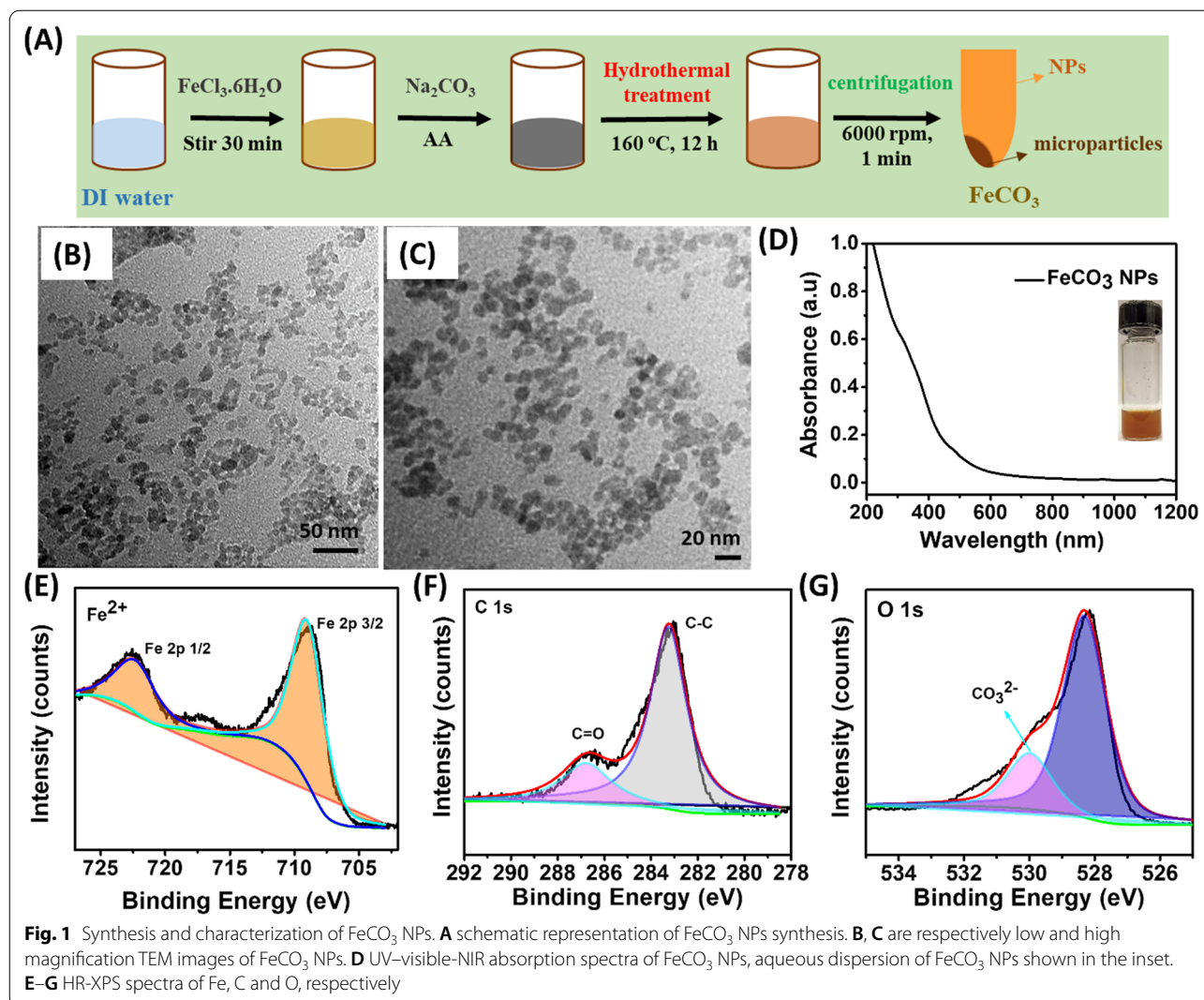
Results and discussion

Synthesis and characterization of $FeCO_3$ NPs

Ultra-fine $FeCO_3$ NPs with an average size of ~ 10 nm were synthesized using a previously reported procedure with a slight modification [30]. The $FeCO_3$ NPs synthesis scheme is shown in detail in Fig. 1A. Previous studies used $FeCO_3$ at the micrometer scale. To achieve smaller $FeCO_3$ NPs, we applied a simple centrifugation separation technique (6000 rpm, 5 min) following hydrothermal treatment, resulting in $FeCO_3$ NPs in a supernatant and $FeCO_3$ microparticles in residue. Microparticle size in the residue was estimated to be > 500 nm, as shown in Additional file 1: Fig. S1. After centrifuging, the resulting $FeCO_3$ NPs were analyzed using high resolution transmission electron microscopy (HR-TEM) to assess morphology, distribution, and average size. As shown in Fig. 1B, C, the HR-TEM image of the $FeCO_3$ NPs reveals that particles are uniform in size and spherical in shape. Notably, individual particle sizes of $FeCO_3$ NPs from TEM analysis are ~ 7 to 8 nm. UV–visible-NIR absorption spectra of the $FeCO_3$ NPs exhibits good optical absorption in the spectral region and the inset shows the optical image of the $FeCO_3$ NPs dispersed in an aqueous solution (Fig. 2D). X-ray photoelectron spectroscopy (XPS) analysis confirmed the structural and phase composition of the resulting $FeCO_3$ NPs. An XPS survey spectrum range of 1200–0 eV shows the clear presence of iron (Fe), carbon (C) and oxygen (O) in the $FeCO_3$ NPs (Additional file 1:Fig. S3). High resolution (HR)-XPS spectra of Fe shows two binding energies at 709 and 722 eV, respectively corresponding to states Fe 2p 3/2 and Fe 2p 1/2, representing Fe in $+2$ oxidation state in $FeCO_3$ NPs (Fig. 1E). HR-XPS spectra of C1s shows two individual peaks with binding energies of 283.1 and 286.7 eV (Fig. 1F). The peak of the lower binding energy is assigned to correspond to C–C or C–H bonding, while the peak of the higher binding energy is assigned to correspond to the carbonate (CO_3^{2-}) peak. However, the peak of the higher binding energy is somewhat shifted to the lower binding energy, possibly due to the interaction of carbonate species with lower oxidation state bonding [31]. As shown in Fig. 1G, the O 1 s spectra region exhibited two distinct peaks with binding energies of 528.2 and 530 eV, respectively corresponding to the −OH and carbonate [32]. Overall, HR-XPS analysis confirmed the final composition of the synthesized nanoparticles are in $FeCO_3$ form.

Magnetic properties of $FeCO_3$ NPs

For MRI applications, contrast agents should possess superparamagnetic behavior and induced relaxation. Thus, the magnetization of $FeCO_3$ NPs was measured at 40.2 emu per gram of Fe (Fig. 2A). The reversible hysteresis curves indicate the superparamagnetic behavior of $FeCO_3$ NPs at room temperature, allowing for biomedical imaging applications. $FeCO_3$ NPs also shows good response to an external magnet (Additional file 1: Fig. S4). Subsequently, the T1 and T2-weighted MR contrast

Thangudu *et al. Journal of Nanobiotechnology*   (2022) 20:157

Page 6 of 13

Fig. 1 Synthesis and characterization of $FeCO_3$ NPs. **A** schematic representation of $FeCO_3$ NPs synthesis. **B**, **C** are respectively low and high magnification TEM images of $FeCO_3$ NPs. **D** UV–visible-NIR absorption spectra of $FeCO_3$ NPs, aqueous dispersion of $FeCO_3$ NPs shown in the inset. **E–G** HR-XPS spectra of Fe, C and O, respectively
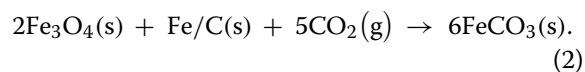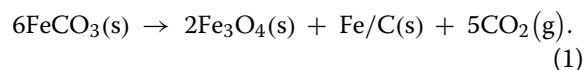
ability of the $FeCO_3$ NPs aqueous solutions was examined using varying concentrations of $FeCO_3$ NPs (with respect to Fe) under a 9.4 T animal MR scanner. As shown in Fig. 2B, T2 weighted MR phantom images of $FeCO_3$ NPs showed significant signal attenuation upon increasing the Fe concentration from 0.0028 mM to 0.0906 mM (Fe concentration in FeCO3 NPs was estimated by using an inductively coupled plasma-mass-spectrometry technique). In contrast, no obvious changes were observed in the T1-weighted MR phantom images even at higher concentrations under otherwise identical conditions. The data clearly indicates that $FeCO_3$ NPs exhibited T2-weighted MR contrast properties, causing the signal intensity of T2-weighted images to gradually decrease as Fe concentrations increase. Plots of signal intensity versus inversion time for the T1/T2-relaxation times with respect to the Fe concentrations are shown in Fig. 2C. The corresponding relaxation rates (r1 = 1/T1 and r2 = 1/

T2) of the $FeCO_3$ NPs exhibit a linear relation to the Fe concentration. The calculated r1 and r2 values for $FeCO_3$ NPs are respectively 3.871 and 730.9 mM^{-1} S^{-1}. Metal carbonates such as $MnCO_3$ nanocrystals exhibit greater contrast in acidic pH than in neutral pH by decomposing the $MnCO_3$ to Mn^{2+} ions. To determine whether this occurs in the $FeCO_3$ NPs, we investigated the pH-dependent MR contrast properties of $FeCO_3$ NPs both in neutral (pH = 7.0) and acidic media (pH = 5.5). As shown in Fig. 2D, no significant changes were observed in the T2-weighted phantom images, indicating no apparent dissolution of $FeCO_3$ NPs. To further we examined the structural and optical changes of $FeCO_3$ NPs by treating with acetate buffer (pH = 5.6). No significant changes were observed in the optical spectra of $FeCO_3$ NPs before and after incubation in acidic condition (acetate buffer, pH = 5.6) for a period of 60 min. Besides, no changes were observed in solution color which reveals that no

Thangudu *et al. Journal of Nanobiotechnology*   (2022) 20:157

Page 7 of 13

Fig. 2 Structural and functional properties of FeCO$_3$ NPs. **A** Magnetic hysteresis loops of FeCO$_3$ NPs at 300 K. **B** T1 and T2-weighted magnetic contrast properties of FeCO$_3$ NPs in aqueous media. **C** r1 and r2 values of FeCO$_3$ NPs with respect to the Fe ion concentration. **D** T2 weighted MRI phantoms of FeCO$_3$ NPs at pH 5.5 and 7.0. **E** r2 relaxivity values of FeCO$_3$ NPs at pH 5.5 and 7.0. **F** Hemolysis assay of FeCO$_3$ NPs at different concentrations, H$_2$O and 0.9% NaCl were respectively used as negative and positive controls (inset show optical images of assay aliquots). **G** T2-weighted MR contrast ability of lung cancer cells in vitro, pre and post-24 h incubation of FeCO$_3$ NPs

possible decomposition of FeCO$_3$ NPs at pH = 5.6 (Additional file 1: Fig. S5A). Subsequently, structural stability of FeCO$_3$ NPs via XPS analysis, shown in (Additional file 1: Fig. S5B–D). Even after treating with acetate buffer (pH = 5.6), high resolution XPS analysis shown a Fe^{2+} and C peaks corresponding to the FeCO$_3$ composition which clearly indicates that Fe^{2+} of FeCO$_3$ NPs is not oxidized into Fe^{3+} at pH 5.6. One of the plausible reasons for the stability of FeCO$_3$ NPs is as follows, FeCO$_3$ decomposition via decarbonated sorbent pathway leads to the formation of Fe$_3$O$_4$, Fe/C and CO$_2$ (Eq. 1) which can re-absorb CO$_2$ to form FeCO$_3$ again (Eq. (2)) [33, 34]. The quick decarbonation and carbonation reactions in FeCO$_3$ facilitates good stability of FeCO$_3$ without

decomposition. However, exact mechanism remains unclear, which is certainly a good topic for future investigations.

$$6FeCO_3(s) \rightarrow 2Fe_3O_4(s) + Fe/C(s) + 5CO_2(g). \tag{1}$$

$$2Fe_3O_4(s) + Fe/C(s) + 5CO_2(g) \rightarrow 6FeCO_3(s). \tag{2}$$

As a result, we did not notice any changes in the r2 values in either medium, and the r2 values of FeCO$_3$ NPs are 730.9 ± 4.8 mM^{-1} S^{-1} in pH = 7.0 and 728.1 ± 5.5 mM^{-1} S^{-1} in pH = 5.5 (Fig. 2E). Notably, we compared the T2-weighted contrast abilities of FeCO$_3$ NPs with FDA-approved clinical contrast agents such

Thangudu *et al. Journal of Nanobiotechnology*   (2022) 20:157

Page 8 of 13

as Resovist® ($r_2 = 374.6 \pm 12.6$ mM^{-1} s^{-1}) [35] and Friedx ($r_2 = 307$ mM^{-1} s^{-1}) [36]. The r2 relaxation value of FeCO$_3$ NPs is 1.95, 2.3 times higher than that of Resovist®, Friedx and FeREX standards under 9.4 T MR system. As discussed earlier, surface coating ligands on FDA-approved contrast agents such as carboxydextran (on Resovist®) [37] and dextran polymer (on Friedx) [37] might result in lower r2 values than that of the FeCO$_3$ NPs. In T2 weighted imaging, T2 contrast agents interact with surrounding water molecules by inducing a local magnetic field. This displays as a relatively "dark" area on T2 weighted images [38]. Most of the carbonate-based nanostructures are porous in nature so which believed to be enabled more water molecules absorb into the pores. Thus, the abundance of more water molecules on FeCO$_3$ NPs surface may help to promote fast proton exchange with water molecules results an enhanced r2 values. The colloidal stability properties of the FeCO$_3$ NPs were studied in different media including water, phosphate buffered saline (PBS) and Dulbecco's Modified Eagle's Medium (DMEM). No significant aggregations were observed in the different media, indicating excellent colloidal stability (Additional file 1: Fig. S6). Prolonged incubation of FeCO$_3$ NPs in aqueous solution also had no effect on stability, with no apparent changes in the absorption spectra (Additional file 1: Fig. S7).

In vitro biocompatibility studies and uptake of FeCO$_3$ NPs

Prior to in vitro and in vivo applications, we evaluated the cytotoxicity and hemocompatibility of the FeCO$_3$ NPs. The in vitro cytotoxicity test was performed on normal cells (human fetal lung fibroblast cells (MRC-5, 1×10^4) using a standard Cell Counting Kit-8 (CCK-8) assay at various concentrations of FeCO$_3$ NPs (0, 10, 25, 50, 75, 100, 150, 200 μg/mL). Results show that FeCO$_3$ NPs had no significant toxic effect on cells during prolonged incubations (24 h and 48 h), and cell viability remained 100% even at higher concentrations (200 μg/mL) (Additional file 1: Fig. S8). This strongly indicates the FeCO$_3$ NPs possess excellent biocompatibility in vitro with no toxicity. No hemolysis activity was detected for different concentrations of FeCO$_3$ NPs, even at 200 μg/mL, indicating that high compatibility with blood cells (Fig. 2F, inset shows assay aliquots images). Water and PBS were respectively used negative and positive controls. Compared to the negative control, a slight degree of hemolysis was found on the FeCO$_3$ NPs, but the hemolysis percentage

remained below 3% at experimental NPs concentrations, verifying their excellent hemocompatibility [39]. Targeting cancer cells with NPs could thus effectively improve the cells' background contrast for MR imaging. Several previous studies have shown that NPs can accumulate in tumors via passive targeting (the so-called Enhanced Permeability and Retention (EPR) effect) based on the difference between specific pathophysiological characteristics of tumors vs healthy tissues [40, 41]. To confirm the cancer cell uptake and passive targeting ability of FeCO$_3$ NPs to further validating MRI performance, CL1-5-luc/GFP lung cancer cells were treated with different concentrations of FeCO$_3$ NPs (0, 0.0145, 0.0725, 0.140 mM, respective to Fe ions) and the in vitro MRI performance was evaluated using a 9.4 T animal MRI system scanner (Fig. 2G). After 24 h of incubation, cells treated with FeCO$_3$ NPs darkened significantly with the increased concentration of NPs corresponding to the T2-weighted contrast with respect to the control group, indicating FeCO$_3$ NPs were successfully internalized in the cancer cells via passive targeting/EPR effect.

T2-weighted MR imaging of in vivo lung tumors

As a proof of concept, we investigated the T2-weighted MR imaging ability of FeCO$_3$ NPs on in vivo lung tumor mice models. Lung tumors were implanted via direct injection of luciferase expressed CL1-5-luc/GFP lung cancer cells (10 μL, 5×10^4) into the lung (experimental setup shown in Additional file 1: Fig. S9A). Two weeks after tumor implantation, lung tumors were identified using IVIS imaging technique (Additional file 1: Fig. S10B). After successful lung tumor formation, FeCO$_3$ NPs were administered intravenously (at a dose of 10 mg/kg of mice) for real-time tracking of in vivo lung tumors using a 9.4 T MR imaging system and compared against a PBS control group. Tumor cells can uptake the NPs via the enhanced permeation and retention (EPR) effect through which NPs are trapped in the tumor tissue through a leaky tumor vasculature and are then retained in the tumor bed due to reduced lymphatic drainage, resulting in successful therapeutics and imaging applications [42–44]. Due to the EPR effect, we observed enhanced T2-weighted MR contrast of in vivo lung tumors after intravenous administration of FeCO$_3$ NPs. Briefly, we acquired T2-weighted MR images of in vivo mice at different time points for FeCO$_3$ NP (pre-injection, post 1 h, 3 h, 5 h) and PBS (pre-injection, post

---

(See figure on next page.)

Fig. 3 In vivo MR contrast properties of FeCO$_3$ NPs. **A** in vivo (n = 3) T2-weighted MR images of lung tumors pre and post-1 h, 3 h, 5 h injection of PBS and FeCO$_3$ NPs (dose of NPs; 10 mg Fe ion/kg, i.v injection, MRI scans were performed on a 9.4 T MRI scanner, circle/pseudo color indicates the tumor region). **B** Kinetic plot of in vivo contrast ability of PBS and FeCO$_3$ NPs, data is represented as mean ± SD; ***P ≤ 0. 001. **C** Schematic representation of in vivo MR imaging of lung tumors using FeCO$_3$ NPs on a 9.4 T MRI scanner

Fig. 3 (See legend on previous page.)
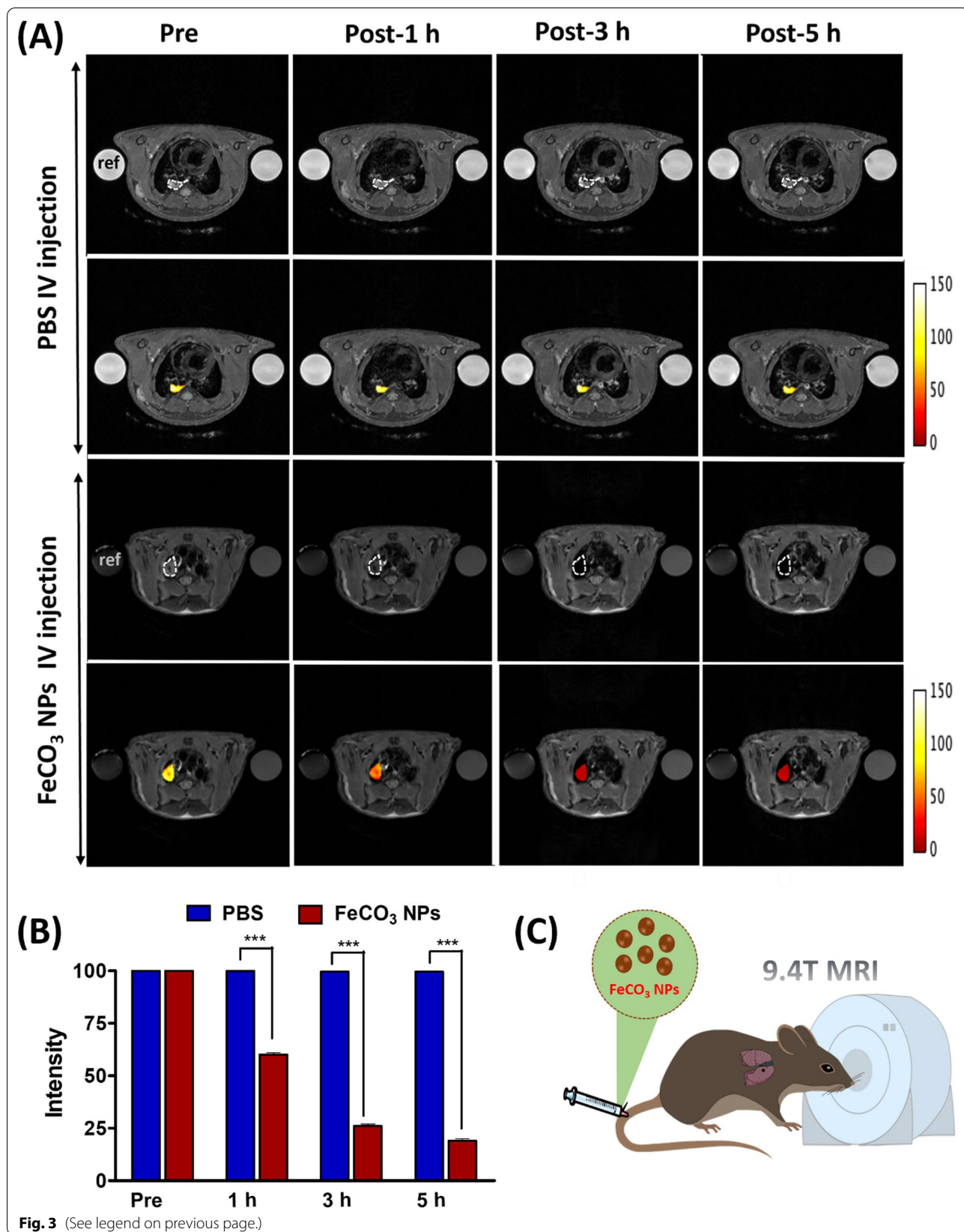
1 h, 3 h, 5 h). As shown in Fig. 3A, FeCO$_3$ NPs began to accumulate in the tumor at 1 h following injection, resulting in a gradual darkening effect corresponding to the T2-weighted contrast observed in the tumor region. Moreover, this T2-weighted contrast in the lung tumor region increased with post FeCO$_3$ NPs injection time from 1 to 5 h. No significant changes in tumor contrast were observed in the PBS group, and all the post injection PBS groups (1 h, 3 h, 5 h) showed the same degree of contrast. To provide statistically significant results, n = 3 mice were used for the in vivo MR imaging investigation of both the FeCO$_3$ NPs and PBS groups (Additional file 1: Figs. S10, S11). We also include color map images in Fig. 3A for clear visibility of tumor contrast in the lung region. We further quantified the signal changes in the lung tumor region through a close analysis of the regions of interest (ROIs) and compared differences between the pre- and post- FeCO$_3$ NPs injection, as well as with the PBS control group (Fig. 3B). Specifically, 55% of the darkening was observed at 1 h and more than ≥ 85% of darkening signal was observed at 3 h and 5 h post-injection of FeCO$_3$ NPs with respect to the pre-injection group. Moreover, the T2 contrast effect of FeCO$_3$ NPs is well maintained in the lung tumor region (1–5 h post-injection), much longer than that of the Gd based complex small molecules (half-life of about several minutes in small animals) [39, 45]. The longer in vivo retention time of the T2 effect on FeCO$_3$ NPs allows for the effective location and study of tumors to obtain and evaluate important pathological information. In contrast, no significant changes were noticed in the lung tumor region of the PBS control group. The schematic representation of the in vivo MR imaging of lung tumors on FeCO$_3$ NPs is shown in Fig. 4C. Overall, in vitro, and in vivo results strongly suggests that the passive targeting of FeCO$_3$ NPs could promote the internalization of more NPs into the tumor cells and exhibit excellent T2-weighted MR contrast for successful visualization/location of in vivo lung tumors.
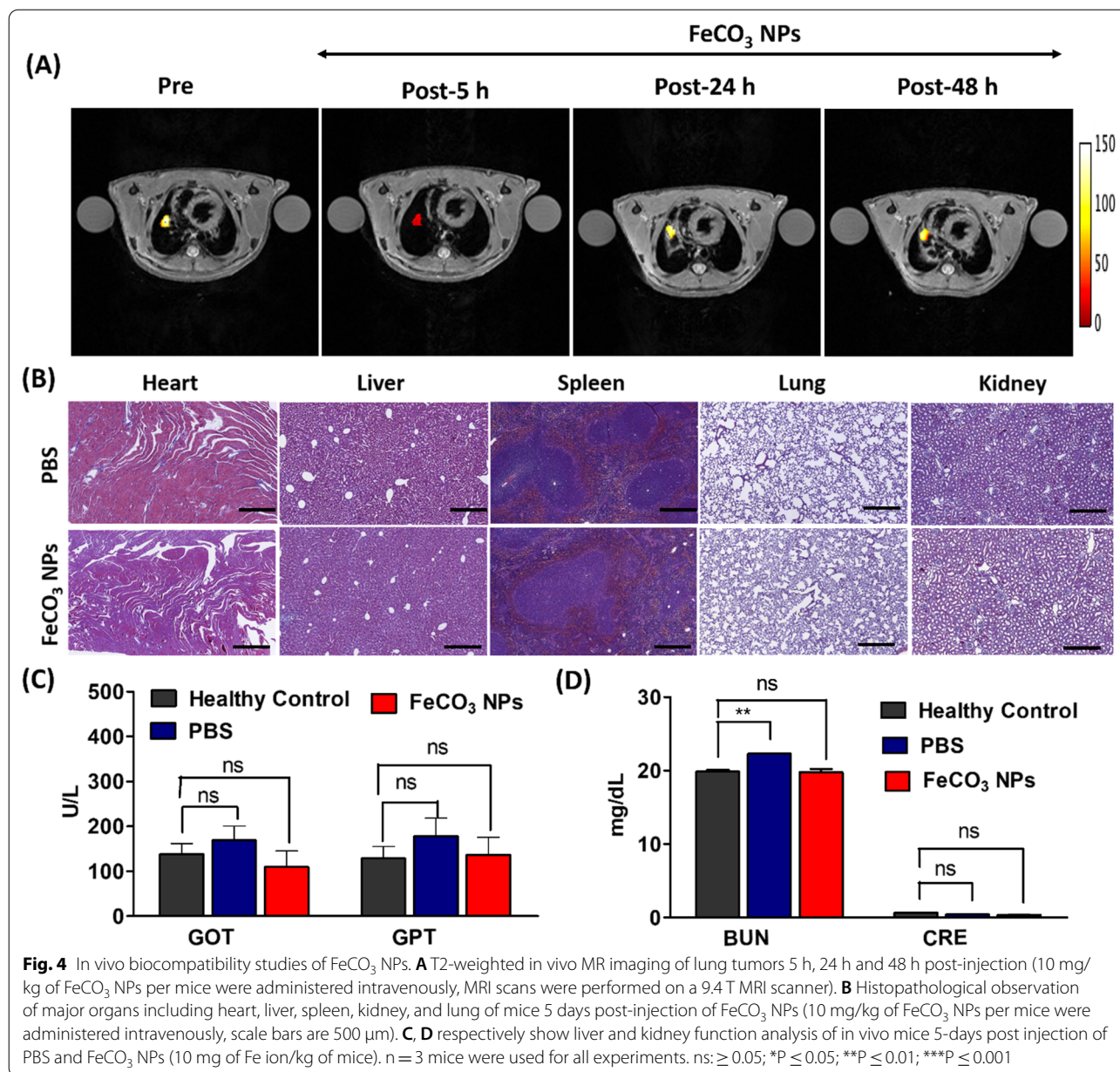
In vivo biocompatibility studies of FeCO$_3$ NPs

Most of the NP-based drugs limit their use in practical/clinical applications due to concerns about chronic accumulation and patient safety [46]. Thus, the USFDA strictly requires NPs to be biodegradable and metabolized or excreted from the body after their intended biomedical applications [46, 47]. Thus, we examined the in vivo potential toxicity and excretion of FeCO$_3$ NPs after intravenous administration into the mice models. As shown in Fig. 4A, MR imaging data reveals the remarkable tumor darkening effect corresponds to the T2 contrast observed after 5 h following FeCO$_3$ NPs injection.

As post-injection time increased to 24 h and 48 h, the tumor contrast gradually increased which strongly indicating that NPs were slowly excreted from the tumor site in the days following injection. We also observed the same phenomenon in the liver region, where accumulation of FeCO$_3$ NPs corresponds to the T2-weighted darkening effect at the initial administration and liver contrast later increased which also strongly confirms the excretion of NPs after a prolonged time following administration (Additional file 1: Fig. S12). Later, hematoxylin and Eosin (H&E) staining analysis results show no histological differences in the major organs 5-days following FeCO$_3$ NPs injection with respect to the control PBS group (Fig. 4B). H&E and in vivo MR imaging studies, indicating good renal clearance from the body following potential MR imaging applications. Serum biochemistry assays were also conducted to investigate the intrinsic toxicities of FeCO$_3$ NPs on major organs such as liver and kidney functions (Fig. 4C, D). We analyzed liver function parameters/indicators such as aspartate aminotransferase (AST/GOT), alanine aminotransferase (ALT/GPT) and kidney function indicators such as serum creatinine (CRE) and blood urea nitrogen (BUN). Five days after FeCO$_3$ NPs injection, no significant changes in liver and kidney functions were observed and all functional values were within the range of the healthy control and PBS control groups, with data respectively shown in Fig. 4C, D. In addition, we also performed the Perl's Prussian blue analysis to detect the presence of iron in tissue samples (Additional file 1: Fig. S13). After 5-day post i.v. injection of FeCO$_3$ NPs, no traces of Fe were observed in the major organs indicating that the successful excretion of NPs after the treatment. Importantly, particle size of NPs are greatly influence on in vivo blood clearance profiles and clearance from body. It was reported that smaller size (5 and 20 nm) of NPs showed rapid clearance from the blood than the larger size (50 nm) NPs after post i.v. injection [48, 49]. Therefore, it was expected that the present smaller size of FeCO$_3$ NPs can be able to clear rapidly from blood since the particle size of FeCO$_3$ NPs are < 20 nm as a result no noticeable side effects or toxicities to major organs. Overall, our biocompatibility results clearly indicate that the as-synthesized FeCO$_3$ NPs exhibited good cyto/hemo compatibility with no obvious toxicity in mice, making them potential candidates for future biomedical MR imaging applications for early diagnosis of lung cancer.

Conclusion

In summary, we have successfully developed the first biocompatible, ultra-small FeCO$_3$ NPs for T2-weighted MR imaging of in vivo lung tumors. FeCO$_3$ NPs

Fig. 4 In vivo biocompatibility studies of FeCO₃ NPs. **A** T2-weighted in vivo MR imaging of lung tumors 5 h, 24 h and 48 h post-injection (10 mg/kg of FeCO₃ NPs per mice were administered intravenously, MRI scans were performed on a 9.4 T MRI scanner). **B** Histopathological observation of major organs including heart, liver, spleen, kidney, and lung of mice 5 days post-injection of FeCO₃ NPs (10 mg/kg of FeCO₃ NPs per mice were administered intravenously, scale bars are 500 µm). **C**, **D** respectively show liver and kidney function analysis of in vivo mice 5-days post injection of PBS and FeCO₃ NPs (10 mg of Fe ion/kg of mice). n = 3 mice were used for all experiments. ns: ≥ 0.05; *P ≤ 0.05; **P ≤ 0.01; ***P ≤ 0.001

exhibited a uniform size distribution, good dispersibility and excellent stability in both aqueous and biological media. Moreover, aqueous solutions of FeCO₃ NPs displayed remarkable T2-weighted MR contrast with a r2 value of $730.9 \pm 4.8 \, mM^{-1} \, S^{-1}$, which is respectively 1.95 and 2.3 times higher than the clinically approved contrast agents Resovist® and Friedx at an identical conditions (under same 9.4 T MR system). Taking advantage of the remarkable T2 contrast abilities, we further demonstrate remarkable T2 contrast ability (≥ 85%) in the tumor region after 5 h post intravenous administration of FeCO₃ NPs. Moreover, the in vivo T2 contrast ability of the FeCO₃ NPs is well maintained in the lung tumor region (1–5 h, after post injection of NPs) compared to Gd-based complex small molecules (half-life of several minutes in small animals). Furthermore, in vitro and in vivo biosafety studies reveal the FeCO₃ NPs are highly biocompatible and no significant toxic effects to the major organs. Overall, the proposed biocompatible FeCO₃ NPs present as a potential candidate for real-time tracking of in vivo lung tumors in future clinical applications for early lung cancer diagnosis.

Thangudu *et al. Journal of Nanobiotechnology*   (2022) 20:157

Page 12 of 13

Supplementary Information

Additional file 1: **Fig. S1**. TEM images of $FeCO_3$ microparticles in the residue; **Fig. S2**. DLS size distribution spectra of $FeCO_3$ NPs. **Fig. S3**. XPS survey spectrum of $FeCO_3$ NPs; Figure S4. $FeCO_3$ NPs in the presence of an external magnetic field; **Fig. S5**. Colloidal stability of FeCO3 NPs in different meda; **Fig. S6**: Absorption spectra of $FeCO_3$ NP aqueous solution before and after 30 days; **Fig. S7**: In vitro cell viability of $FeCO_3$ NPs in MRC-5 normal cells; Figure S8: Lung tumor implantation setup; **Figs. S9 and S10**: In vivo T2-weighted MR images of mice models (n $=$ 3) after injection of PBS and $FeCO_3$ NPs respectively; **Fig. S11**: In vivo T2-weighted contrast of liver after injection of $FeCO_3$ NPs; **Table S1**. Comparison of image modalities used in molecular imaging.

Authors' contributions
ST and SCH conceived the idea and designed the experiments. ST conducted the preparation and characterization. ST and CCY performed the relaxivity measurements and data analysis both in vitro and in vivo. ST, CLL, MCL performed the biodistribution analysis. ST and SCH wrote the manuscript. All authors read and approved the final manuscript.

Availability of data and materials
All supporting data for this study are included in this published article and its additional information files. All the experimental protocols involving live animals were reviewed and approved by the Institutional Animal Care and Use Committee (IACUC No. 2021031802) of Chang Gung Memorial Hospital and were performed in accordance with the Animal Protection Regulations of the Council of Agriculture, Executive Yuan (R.O.C.) and the guidelines of the National Research Council (U.S.A.) for the care and use of laboratory animals.

Declarations

Ethics approval and consent to participate
All the experimental protocols involving live animals were reviewed and approved by the Institutional Animal Care and Use Committee (IACUC No. 2021031802) of Chang Gung Memorial Hospital and were performed in accordance with the Animal Protection Regulations of the Council of Agriculture, Executive Yuan (R.O.C.) and the guidelines of the National Research Council (U.S.A.) for the care and use of laboratory animals.

Consent for publication
All authors agree to publish this manuscript.

Competing interests
The authors declare no competing financial interest.

Author details
[1]Institute for Translational Research in Biomedicine, Kaohsiung Chang Gung Memorial Hospital, Kaohsiung 833, Taiwan. [2]Department of Biomedical Imaging and Radiological Sciences, National Yang Ming Chiao Tung University, Taipei 112, Taiwan. [3]Center for General Education, Chang Gung University, Taoyuan 333, Taiwan.

References

1. Bray F, Ferlay J, Soerjomataram I, Siegel RL, Torre LA, Jemal A. Global cancer statistics 2018: GLOBOCAN estimates of incidence and mortality worldwide for 36 cancers in 185 countries. CA Cancer J Clin. 2018;68:394–424.
2. El-Sherif A, Gooding WE, Santos R, Pettiford B, Ferson PF, Fernando HC, Urda SJ, Luketich JD, Landreneau RJ. Outcomes of sublobar resection versus lobectomy for stage I non-small cell lung cancer: a 13-year analysis. Ann Thorac Surg. 2006;82:408–15 (**discussion 415–406**).
3. Videtic GMM, Donington J, Giuliani M, Heinzerling J, Karas TZ, Kelsey CR, Lally BE, Latzka K, Lo SS, Moghanaki D, et al. Stereotactic body radiation therapy for early-stage non-small cell lung cancer: executive summary of an ASTRO evidence-based guideline. Pract Radiat Oncol. 2017;7:295–301.
4. Frangioni JV. New technologies for human cancer imaging. J Clin Oncol. 2008;26:4012–21.
5. Haris M, Yadav SK, Rizwan A, Singh A, Wang E, Hariharan H, Reddy R, Marincola FM. Molecular magnetic resonance imaging in cancer. J Transl Med. 2015;13:313.
6. Su C-H, Hsu Y-C, Thangudu S, Chen W-Y, Huang Y-T, Yu C-C, Shih Y-H, Wang C-J, Lin C-L. Application of multiparametric MR imaging to predict the diversification of renal function in miR29a-mediated diabetic nephropathy. Sci Rep. 1909;2021:11.
7. Major JL, Meade TJ. Bioresponsive, cell-penetrating, and multimeric MR contrast agents. Acc Chem Res. 2009;42:893–903.
8. Xiao Y-D, Paudel R, Liu J, Ma C, Zhang Z-S, Zhou S-K. MRI contrast agents: classification and application (review). Int J Mol Med. 2016;38:1319–26.
9. Yang C-T, Chuang K-H. Gd(iii) chelates for MRI contrast agents: from high relaxivity to "smart", from blood pool to blood–brain barrier permeable. MedChemComm. 2012;3:552–65.
10. Kanda T, Nakai Y, Oba H, Toyoda K, Kitajima K, Furui S. Gadolinium deposition in the brain. Magn Reson Imaging. 2016;34:1346–50.
11. Ramalho J, Semelka RC, Ramalho M, Nunes RH, AlObaidy M, Castillo M. Gadolinium-based contrast agent accumulation and toxicity: an update. Am J Neuroradiol. 2016;37:1192–8.
12. Shen Z, Wu A, Chen X. Iron oxide nanoparticle based contrast agents for magnetic resonance imaging. Mol Pharm. 2017;14:1352–64.
13. Su C-H, Tsai C-Y, Tomanek B, Chen W-Y, Cheng F-Y. Evaluation of blood–brain barrier-stealth nanocomposites for in situ glioblastoma theranostics applications. Nanoscale. 2016;8:7866–70.
14. Wang Y-XJ. Superparamagnetic iron oxide based MRI contrast agents: current status of clinical application. Quant Imag Med Surg. 2011;1:35–40.
15. Wáng YXJ, Idée J-M. A comprehensive literatures update of clinical researches of superparamagnetic resonance iron oxide nanoparticles for magnetic resonance imaging. Quant Imaging Med Surg. 2017;7:88–122.
16. Bobo D, Robinson KJ, Islam J, Thurecht KJ, Corrie SR. Nanoparticle-based medicines: a review of FDA-approved materials and clinical trials to date. Pharm Res. 2016;33:2373–87.
17. Palui G, Aldeek F, Wang W, Mattoussi H. Strategies for interfacing inorganic nanocrystals with biological systems based on polymer-coating. Chem Soc Rev. 2015;44:193–227.
18. Gupta AK, Gupta M. Synthesis and surface engineering of iron oxide nanoparticles for biomedical applications. Biomaterials. 2005;26:3995–4021.
19. Arami H, Khandhar A, Liggitt D, Krishnan KM. In vivo delivery, pharmacokinetics, biodistribution and toxicity of iron oxide nanoparticles. Chem Soc Rev. 2015;44:8576–607.
20. Tong S, Hou S, Zheng Z, Zhou J, Bao G. Coating optimization of superparamagnetic iron oxide nanoparticles for high T2 relaxivity. Nano Lett. 2010;10:4607–13.
21. d'Amora M, Liendo F, Deorsola FA, Bensaid S, Giordani S. Toxicological profile of calcium carbonate nanoparticles for industrial applications. Colloids Surf B Biointerfaces. 2020;190:110947.
22. Maleki Dizaj S, Barzegar-Jalali M, Zarrintan MH, Adibkia K, Lotfipour F. Calcium carbonate nanoparticles as cancer drug delivery system. Expert Opin Drug Deliv. 2015;12:1649–60.

Thangudu *et al. Journal of Nanobiotechnology*   (2022) 20:157

Page 13 of 13

23. Xue P, Hou M, Sun L, Li Q, Zhang L, Xu Z, Kang Y. Calcium-carbonate packaging magnetic polydopamine nanoparticles loaded with indocyanine green for near-infrared induced photothermal/photodynamic therapy. Acta Biomater. 2018;81:242–55.

24. Dong Z, Feng L, Zhu W, Sun X, Gao M, Zhao H, Chao Y, Liu Z. CaCO(3) nanoparticles as an ultra-sensitive tumor-pH-responsive nanoplatform enabling real-time drug release monitoring and cancer combination therapy. Biomaterials. 2016;110:60–70.

25. Wei Z, Lin X, Wu M, Zhao B, Lin R, Zhang D, Zhang Y, Liu G, Liu X, Liu J. Core-shell NaGdF4@CaCO3 nanoparticles for enhanced magnetic resonance/ultrasonic dual-modal imaging via tumor acidic micro-enviroment triggering. Sci Rep. 2017;7:5370.

26. Wang M, Zhou B, Wang L, Zhou F, Smith N, Saunders D, Towner RA, Song J, Qu J, Chen WR. Biodegradable pH-responsive amorphous calcium carbonate nanoparticles as immunoadjuvants for multimodal imaging and enhanced photoimmunotherapy. J Mater Chem B. 2020;8:8261–70.

27. Cheng Y, Zhang S, Kang N, Huang J, Lv X, Wen K, Ye S, Chen Z, Zhou X, Ren L. Polydopamine-coated manganese carbonate nanoparticles for amplified magnetic resonance imaging-guided photothermal therapy. ACS Appl Mater Interfaces. 2017;9:19296–306.

28. Zhu X, Xiong H, Zhou Q, Zhao Z, Zhang Y, Li Y, Wang S, Shi S. A pH-activatable $MnCO_3$ nanoparticle for improved magnetic resonance imaging of tumor malignancy and metastasis. ACS Appl Mater Interfaces. 2021;13:18462–71.

29. Wang M, Bao T, Yan W, Fang D, Yu Y, Liu Z, Yin G, Wan M, Mao C, Shi D. Nanomotor-based adsorbent for blood Lead(II) removal in vitro and in pig models. Bioactive Mater. 2021;6:1140–9.

30. Zhang F, Zhang R, Feng J, Ci L, Xiong S, Yang J, Qian Y, Li L. One-pot solvothermal synthesis of graphene wrapped rice-like ferrous carbonate nanoparticles as anode materials for high energy lithium-ion batteries. Nanoscale. 2015;7:232–9.

31. Liu F, Csetenyi L, Gadd GM. Amino acid secretion influences the size and composition of copper carbonate nanoparticles synthesized by ureolytic fungi. Appl Microbiol Biotechnol. 2019;103:7217–30.

32. Ji Y, Ma M, Ji X, Xiong X, Sun X. Nickel-carbonate nanowire array: an efficient and durable electrocatalyst for water oxidation under nearly neutral conditions. Front Chem Sci Eng. 2018;12:467–72.

33. Cerantola V, Bykova E, Kupenko I, Merlini M, Ismailova L, McCammon C, Bykov M, Chumakov AI, Petitgirard S, Kantor I, et al. Stability of iron-bearing carbonates in the deep Earth's interior. Nat Commun. 2017;8:15960.

34. Mora Mendoza EY, Sarmiento Santos A, Vera López E, Drozd V, Durygin A, Chen J, Saxena SK. Iron oxides as efficient sorbents for CO_2 capture. J Market Res. 2019;8:2944–56.

35. Jedlovszky-Hajdú A, Tombácz E, Bányai I, Babos M, Palkó A. Carboxylated magnetic nanoparticles as MRI contrast agents: relaxation measurements at different field strengths. J Magn Magn Mater. 2012;324:3173–80.

36. Wu Y, Zhang R, Tran HDN, Kurniawan ND, Moonshi SS, Whittaker AK, Ta HT. Chitosan nanococktails containing both ceria and superparamagnetic iron oxide nanoparticles for reactive oxygen species-related theranostics. ACS Appl Nano Mater. 2021;4:3604–18.

37. Mailänder V, Lorenz MR, Holzapfel V, Musyanovych A, Fuchs K, Wiesneth M, Walther P, Landfester K, Schrezenmeier H. Carboxylated superparamagnetic iron oxide particles label cells intracellularly without transfection agents. Mol Imaging Biol. 2008;10:138–46.

38. Cowger TA, Tang W, Zhen Z, Hu K, Rink DE, Todd TJ, Wang GD, Zhang W, Chen H, Xie J. Casein-coated Fe_5C_2 nanoparticles with superior r2 relaxivity for liver-specific magnetic resonance imaging. Theranostics. 2015;5:1225–32.

39. Wu C, Cai R, Zhao T, Wu L, Zhang L, Jin J, Xu L, Li P, Li T, Zhang M, Du F. Hyaluronic acid-functionalized gadolinium oxide nanoparticles for magnetic resonance imaging-guided radiotherapy of tumors. Nanoscale Res Lett. 2020;15:94.

40. Park J, Choi Y, Chang H, Um W, Ryu JH, Kwon IC. Alliance with EPR effect: combined strategies to improve the EPR effect in the tumor microenvironment. Theranostics. 2019;9:8073–90.

41. Nakamura Y, Mochida A, Choyke PL, Kobayashi H. Nanodrug delivery: is the enhanced permeability and retention effect sufficient for curing cancer? Bioconjug Chem. 2016;27:2225–38.

42. Fang J, Nakamura H, Maeda H. The EPR effect: unique features of tumor blood vessels for drug delivery, factors involved, and limitations and augmentation of the effect. Adv Drug Deliv Rev. 2011;63:136–51.

43. Man F, Lammers T, DeRosales RTM. Imaging nanomedicine-based drug delivery: a review of clinical studies. Mol Imag Biol. 2018;20:683–95.

44. Thangudu S, Cheng F-Y, Su C-H. Advancements in the blood–brain barrier penetrating nanoplatforms for brain related disease diagnostics and therapeutic applications. Polymers. 2020;12:3055.

45. Zhou H, Tang J, Li J, Li W, Liu Y, Chen C. In vivo aggregation-induced transition between T(1) and T(2) relaxations of magnetic ultra-small iron oxide nanoparticles in tumor microenvironment. Nanoscale. 2017;9:3040–50.

46. Choi HS, Frangioni JV. Nanoparticles for biomedical imaging: fundamentals of clinical translation. Mol Imag. 2010;9:291–310.

47. Poon W, Zhang Y-N, Ouyang B, Kingston BR, Wu JLY, Wilhelm S, Chan WCW. Elimination pathways of nanoparticles. ACS Nano. 2019;13:5785–98.

48. Xia Q, Huang J, Feng Q, Chen X, Liu X, Li X, Zhang T, Xiao S, Li H, Zhong Z, Xiao K. Size- and cell type-dependent cellular uptake, cytotoxicity and in vivo distribution of gold nanoparticles. Int J Nanomed. 2019;14:6957–70.

49. Hoshyar N, Gray S, Han H, Bao G. The effect of nanoparticle size on in vivo pharmacokinetics and cellular interaction. Nanomedicine. 2016;11:673–92.

Publisher's Note

Springer Nature remains neutral with regard to jurisdictional claims in published maps and institutional affiliations.